



OPEN

SUBJECT AREAS:

PHASE TRANSITIONS
AND CRITICAL
PHENOMENA

TWO-DIMENSIONAL MATERIALS

MAGNETIC PROPERTIES AND
MATERIALSSURFACES, INTERFACES AND
THIN FILMSReceived
14 March 2014Accepted
27 June 2014Published
17 July 2014Correspondence and
requests for materials
should be addressed toJ.T. (j-tominaga@aist.
go.jp)

Mirror-symmetric Magneto-optical Kerr Rotation using Visible Light in $[(\text{GeTe})_2(\text{Sb}_2\text{Te}_3)_1]_n$ Topological Superlattices

Do Bang¹, Hiroyuki Awano¹, Junji Tominaga², Alexander V. Kolobov², Paul Fons², Yuta Saito², Kotaro Makino², Takashi Nakano², Muneaki Hase³, Yukihiko Takagaki⁴, Alessandro Giussani⁴, Raffaella Calarco⁴ & Shuichi Murakami⁵

¹Information Storage Materials Laboratory, Toyota Technological Institute, Nagoya, Japan, ²Nanoelectronics Research Institute, National Institute of Advanced Industrial Science & Technology (AIST), Tsukuba, Japan, ³Faculty of Pure and Applied Science, University of Tsukuba, Tsukuba, Japan, ⁴Paul-Drude-Institut für Festkörperelektronik, Berlin, Germany, ⁵Department of Physics, TIES, Tokyo Institute of Technology, Tokyo, Japan.

Interfacial phase change memory (iPCM), that has a structure of a superlattice made of alternating atomically thin GeTe and Sb_2Te_3 layers, has recently attracted attention not only due to its superior performance compared to the alloy of the same average composition in terms of energy consumption but also due to its strong response to an external magnetic field (giant magnetoresistance) that has been speculated to arise from switching between topological insulator (RESET) and normal insulator (SET) phases. Here we report magneto-optical Kerr rotation loops in the visible range, that have mirror symmetric resonances with respect to the magnetic field polarity at temperatures above 380 K when the material is in the SET phase that has Kramers-pairs in spin-split bands. We further found that this threshold temperature may be controlled if the sample was cooled in a magnetic field. The observed results open new possibilities for use of iPCM beyond phase-change memory applications.

Topological insulators (TIs) have attracted increasing attention from both solid-state physics and applications in spintronics devices perspectives^{1–5}. TIs such as Sb_2Te_3 and related chalcogenides built from quintuple layers (QL) satisfy both spatial inversion symmetry and time reversal symmetry, resulting in a single Dirac cone at the Γ point^{6,7}, where the spin bands are degenerate due to the presence of inversion symmetry. However, once spatial symmetry is broken, e.g. by an external electric field, the band gap opens and the spin degeneracy is lifted resulting in a Rashba-split phase⁸. To date, experimental studies of TI properties have usually been carried out using single crystal surfaces in vacuum^{4,6}.

Recently, it was predicted that interfacial phase change memory (iPCM)⁹, which consists of a superlattice with alternating Sb_2Te_3 (TI) and normal insulating (NL) GeTe spacer layers: $[(\text{GeTe})_2(\text{Sb}_2\text{Te}_3)_1]_n$, where l and n are integers¹⁰, originally developed with the objective to reduce energy consumption, may exist in different topological phases¹¹. In particular, it was argued that iPCM with $l = 1$ was a Dirac semimetal with bulk gapless states¹². Furthermore, electric-field induced giant magnetoresistance was experimentally observed at room temperature despite no magnetic elements being included¹³. It has been speculated that this phenomena is caused by the Rashba effect due to the breaking of spatial inversion symmetry¹².

In this work we report on optical detection of topological properties of iPCM, in particular, on the use of the magneto-optical Kerr rotation. Magneto-optical phenomena such as Kerr- or Faraday-rotation were proposed to be alternative tools to probe the spin-dependent response of TIs, besides the spin transport analysis^{14,15}. The rather simple polar-Kerr-rotation technique, where linear polarized light and an external magnetic field are both applied normal to a sample surface, is especially appealing¹⁶. The light induces an AC electrical field in the illuminated spot along the polarization direction, generating a time dependent Hall conductance $\sigma_{xy}(t)$, which affects the off-diagonal elements of the dielectric tensor ϵ_{ij} ($i, j = x, y, z$) as the dielectric constant arises from the electrical conductance σ_{ij} within the framework of Kubo's linear response theory¹⁷. Recently, Faraday and Kerr-rotation on



TI surfaces were theoretically discussed¹⁸, and it was predicted that a resonant condition may induce a giant Kerr rotation θ_K by $-\pi/2$ radian in the low frequency (terahertz) range for a wavelength far longer than the TI film thickness¹⁸. Here we demonstrate that this approach is not limited to the resonance between the broken Dirac cone bands that form the band gap between the filled and empty states but even using visible light, where absorption involves transitions between the valence spin bands and higher conduction bands, a large Kerr-rotation can be observed.

Results

SET&RESET structures of interfacial phase change memory (iPCM). Figure 1(a) shows two iPCM phases (the high-conductivity SET and low-conductivity RESET phases), the corresponding electronic band structures calculated including spin-orbit coupling (SOC) effects in bulk¹² (See Method), and the high-angle annular dark field transmission electron microscope (HAADF-TEM) images of the RESET and SET phases of the iPCM $[(\text{GeTe})_2(\text{Sb}_2\text{Te}_3)]_{20}$ structure fabricated at 520 K on a Si substrate. The RESET phase has spatial inversion symmetry with a Dirac cone in the bulk while the SET phase doesn't. The SET and RESET phases reversibly transform into each other within a temperature range of 380 K and 450 K as shown in Figure 1(b), where the temperature dependence of the resistance of iPCM is shown. The shown behavior is highly unusual for phase-change memory where the change of resistance upon cooling the SET phase is typically negligible¹⁹. It should also be noted, that iPCM in the SET state has an unusually structured

optical absorption spectrum in the visible wavelength range as shown in Fig. 1(c). In particular, despite a rather small band gap of ~ 0.3 eV, the SET phase exhibits a sharp absorption increase near 700-nm, which corresponds to transitions from below the Fermi level to unoccupied energy bands located ca. 1.8 eV (690 nm) above the Fermi level (see the band structure of the SET phase in Fig. 1(a)). In contrast with the band structure in the RESET phase, the spin degeneracy is lifted in the SET phase by the breaking of spatial inversion symmetry generating a narrow band gap, while the phase still preserves the time reversal symmetry.

Mirror-symmetric Kerr-rotation of iPCM thin films. Polar Kerr-rotation results of the RESET and SET phases of $[(\text{GeTe})_2(\text{Sb}_2\text{Te}_3)]_{20}$ iPCM obtained using 690-nm light are shown in Fig. 2 (a), measured at room temperature and at 440 K (See Method). While the signal at room temperature was within noise, a strong and unusual Kerr-loop with $\theta_K \sim -0.3$ degree was observed at 440 K within the applied magnetic field range (± 13 kOe). The loop has four resonances with a mirror-symmetry completely dissimilar to the deformed-rectangular hysteresis loop with respect to the magnetic field polarity typically observed in ferromagnetic materials. The drawing order of the shown curve is as follows: $0 \rightarrow 1 \rightarrow 2 \rightarrow 3 \rightarrow 4 \rightarrow 5(0) \rightarrow 6 \rightarrow 7 \rightarrow 8 \rightarrow 9 \rightarrow 0$. The magnetic field required to generate resonance peaks 1 and 3 monotonically increased with decreasing temperature as shown in Fig. 2(b). Once the temperature was decreased to less than the threshold (~ 380 K), the signals disappeared abruptly, but reappeared reversibly when the temperature was increased again

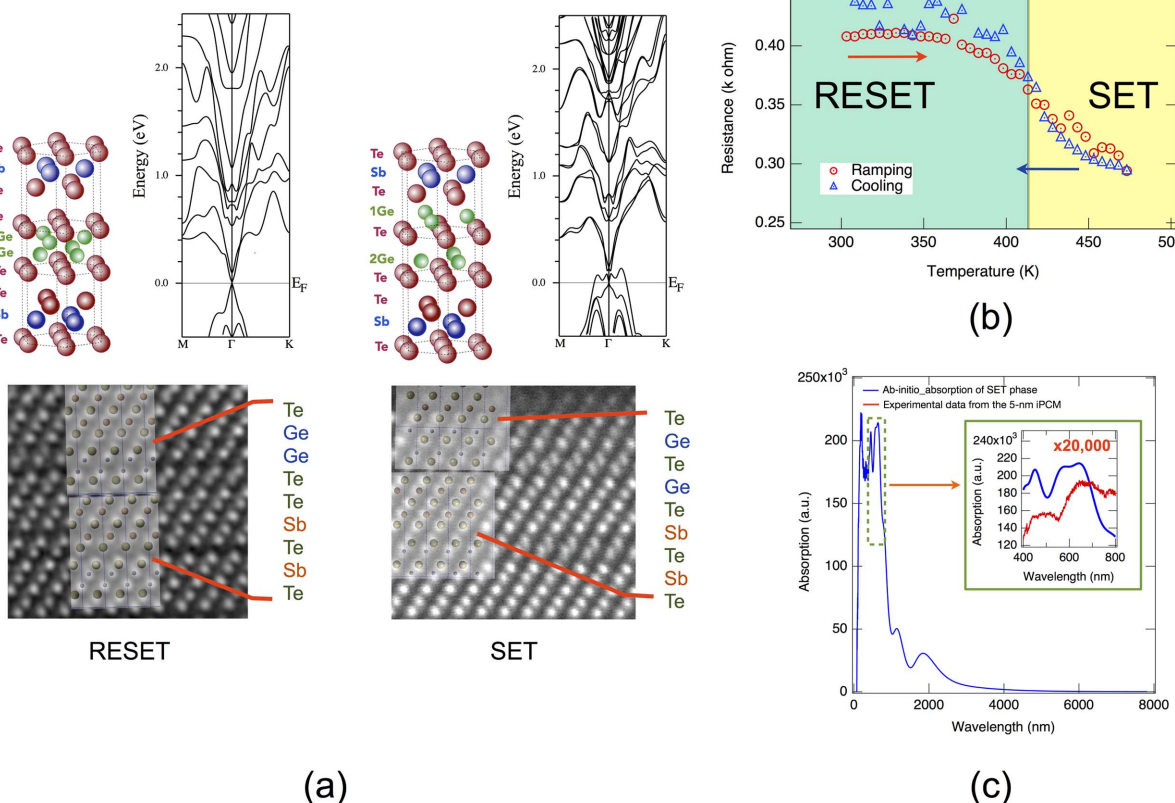


Figure 1 | (a) Two different crystalline phases (RESET and SET) of iPCM $[(\text{GeTe})_2(\text{Sb}_2\text{Te}_3)]_n$, the corresponding band structures (only shown in M- Γ -K k-space) calculated by *ab-initio* computer simulations, and high-angle annular dark field transmission electron microscope (HAADF-TEM) images of the real RESET and SET phases with superimposed simulation models. Sb_2Te_3 -quintuple layers and $(\text{GeTe})_2$ layers were clearly identified as well as a vacancy layer, respectively. The spin-bands are degenerate in the RESET phase while the degeneracy is lifted in the SET phase. (b) Temperature dependence of the resistance upon heating (red) & cooling (blue) demonstrating a reversible change, using a $[(\text{GeTe})_2(\text{Sb}_2\text{Te}_3)]_{n=20}$ superlattice film. (c) Optical absorption of the SET phase calculated using *ab-initio* computer simulations (blue), and the zoom of the visible wavelength range (inset) with an experimentally observed curve using a $[(\text{GeTe})_2(\text{Sb}_2\text{Te}_3)]_{n=2}$ superlattice film.

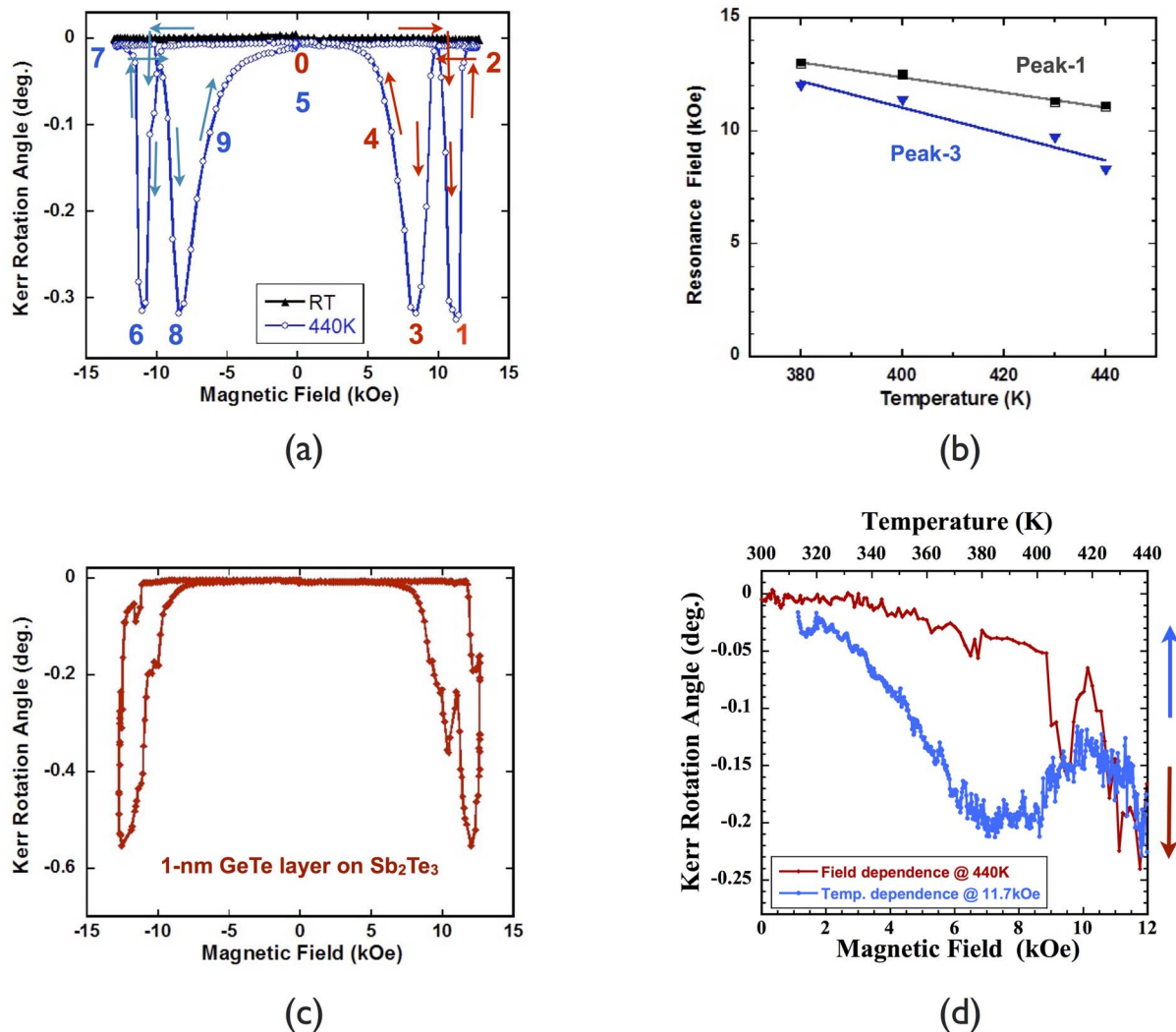


Figure 2 | (a) Mirror-symmetric Kerr-loop observed from iPCM $[(\text{GeTe})_2(\text{Sb}_2\text{Te}_3)]_{20}$ structure at 440 K (blue). For comparison the result of the room temperature measurement is shown in black. The order of the Kerr signal with variation in magnetic field was: 0 → 1 → 2 → 3 → 4 → 5(0) → 6 → 7 → 8 → 9 → 0; (b) Magnetic fields corresponding to 1 and 3 resonances as a function of temperature; below 380 K the Kerr rotation disappears; (c) The Kerr-loop arising from an 1-nm thick $(\text{GeTe})_2$ layer on top of a 5-nm Sb_2Te_3 layer (used to orient GeTe) at 440 K; (d) Kerr-signal behavior of (c) due to a magnetic field at 440 K (red) and by cooling the sample temperature at 11.85 kOe (blue). 0 to 9 and arrows marked on the loop in (a) are the order of one Kerr-loop cycle.

above the threshold. The threshold temperature for the (dis)appearance of the Kerr-signal is in good agreement with the transition temperature between the SET and RESET phases observed in the electrical resistance measurements (Fig. 1(b)), suggesting that the observed Kerr loops are associated with the SET phase.

The sense of the Kerr rotation changed randomly for various samples and even different pieces of nominally the same sample but the mirror symmetry and the threshold nature of the Kerr rotation were reproduced for all samples. We further found that the signal intensity dropped significantly when the light wavelength was changed from 690-nm to 650-nm (Fig. S1). At the same time the magnetic field at which the resonant Kerr rotation occurred shifted to a lower value for the light with a higher photon energy suggesting that the photon energy and Zeeman splitting add up to generate the necessary conditions for the Kerr rotation resonance. The Kerr rotation angle became negligibly small for 400-nm light, further demonstrating that the process has a resonant nature.

To study the origin of the magneto-optical response in iPCM, we also examined the phenomena using several different films. As shown in Fig. 2(c), a 1-nm thick GeTe layer fabricated on a 5-nm

thick Sb_2Te_3 layer (required to orient the growth along the $\langle 111 \rangle$ direction) showed similar loops at 440 K. At the same time, the Sb_2Te_3 layer alone, and a 20-nm thick epitaxial GeTe layer grown on Si (111) did not exhibit any measurable signal. This result underscores the important role of $\text{GeTe}/\text{Sb}_2\text{Te}_3$ interfaces in the observed effect, similar to the case of the giant magnetoresistance observed in iPCM but not in alloyed materials of the same average composition¹³. It is worth noting that the two resonance drops for the GeTe layer shown in Fig. 2(c) merge into one demonstrating a rather small hysteresis, compared to the much larger hysteresis in $[(\text{GeTe})_2(\text{Sb}_2\text{Te}_3)]_{20}$, a result that suggests that the superlattice is ferro-magnetized and has the potential to store spin in the heterostructure due to proximity-induced interfacial magnetization^{20,21}.

It is interesting to note that, when the 1-nm thick GeTe layer on the 5-nm thick Sb_2Te_3 layer was cooled under the applied magnetic field, the Kerr loop could be observed down to 320 K, i.e. 60 degrees lower than the threshold temperature without the magnetic field (Fig. 2(d)); the same phenomenon was observed in $[(\text{GeTe})_2(\text{Sb}_2\text{Te}_3)]_{20}$ down to 310 K as well (not shown), i.e. the phase transition between SET and RESET could be controlled by the external magnetic field.



Magneto-electric effect in the RESET phase. Although the RESET phase does not exhibit Kerr rotation, it also has a specific response to the applied magnetic field. As shown in Fig. 3, the optical dielectric constant of the $[(\text{GeTe})_2(\text{Sb}_2\text{Te}_3)_1]_{20}$ film at room temperature was increased in the region, where the magnetic field (4 kOe) was applied. In the Maxwell equations, a static magnetic field does not couple to a dielectric constant. This phenomenon is highly unusual, except for a few multiferroic composites with highly-oriented interfacial contact of ferromagnetic and ferroelectric thin films^{22,23}.

Discussions

We now address a possible mechanism for the observed phenomenon. While the accurate description of the observed results requires further study, the basic results can be understood as follows. As shown in Fig. 1(a), the degeneracy of the spin-bands in the SET phase is lifted due to the breaking of spatial inversion symmetry by the phase transition from RESET to SET states.

Before we discuss the origin of the Kerr-loop in the SET phase, we consider the system in the RESET phase that possesses both time reversal and spatial inversion symmetries. In the absence of an external magnetic field, the up-spin (\uparrow) and down-spin (\downarrow) electrons satisfy the condition $E(-\mathbf{k}, \downarrow) = E(+\mathbf{k}, \uparrow)$, where E and \mathbf{k} are band energy and electron momentum, respectively. Since in a two-dimensional system with the Dirac cone spins are usually oriented in plane²⁴, it may be more appropriate to re-write the above condition as $E(-\mathbf{k}, \leftarrow) = E(+\mathbf{k}, \rightarrow)$. Because the energy of the spin-orbit interaction is $\propto (\sigma_x \mathbf{k}_y - \sigma_y \mathbf{k}_x) E_z$, where σ_x and σ_y are Pauli spin matrices, and E_z is the z-component of the electrical field induced by the laser beam (the z-direction is defined to be normal to the sample surface), it is essentially impossible for our laser set-up with just four degree away from normal incidence to induce a strong E_z lifting of the band degeneracy in the RESET phase shown in Fig. 1(a). Even for the case that the actual film surface is not perfectly normal to E_z , Kerr-rotation components θ_{K+} and θ_{K-} cancel each other due to the presence of degeneracy.

When time reversal symmetry is broken by an application of an external magnetic field $B_z(\uparrow)_{\text{ex}}$ or $B_z(\downarrow)_{\text{ex}}$, the situation becomes different due to the Zeeman effect. The Zeeman effect in a thin film topological insulator was recently theoretically investigated for the case when an external magnetic field was applied normal to the surface^{25,26}. The magnitude depends on the hybridization energy of the helical spins between the top and bottom surfaces of the thin film topological insulator. Although the Zeeman energy $\Delta z = 1/2 \cdot g \mu_B B$ is usually small, it is noted here that in the presence of large spin-orbit coupling, the Lande factor g of topological insulators can be rather

large, over 50 for Bi_2Se_3 , which corresponds to Δz of a few tens meV^{27,28}. Since the helical spin coupling between the top and bottom interfaces in the superlattice and spin-orbit coupling give rise to a Dirac cone in the bulk state in the $[(\text{GeTe})_2(\text{Sb}_2\text{Te}_3)_1]_{20}$ iPCM film¹², a large Zeeman effect can also be expected by analogy in our case. The large change between the band structures originates from the helical spin coupling. In addition, it was theoretically reported that a superlattice structure built from $[(\text{BiTe})_l(\text{Bi}_2\text{Te}_3)_m]$ blocks, where l and m are integers, also has a large Rashba splitting due to the breaking of spatial inversion symmetry, which leads to an out-of-plane spin component (z)²⁹. The Zeeman energy shift may thus be comparable to the band split (~ 50 meV) near 1.8 eV corresponding to the laser wavelength (690 nm) as shown in the SET phase (Fig. 1(a)). The magneto-optical effect shown in Fig. 3 is presumably attributed to the Zeeman effect in the iPCM film.

Due to the combination of the Zeeman effect and the breaking of time reversal symmetry, two different cases can be considered depending on the direction of the external magnetic fields: $B_z(\uparrow)_{\text{ex}}$ and $B_z(\downarrow)_{\text{ex}}$. As the internal magnetic field from the spin-orbit coupling is added to the $B_z(\uparrow \text{ or } \downarrow)_{\text{ex}}$ in the superlattice, hereafter we use the effective magnetic field, $B_z(\uparrow \text{ or } \downarrow)_{\text{eff}}$. For increasing $B_z(\uparrow)_{\text{ex}}$, the energy balance between spin-up and spin-down bands is changed to $E(-\mathbf{k}, \downarrow) > E(+\mathbf{k}, \uparrow)$, as shown in Fig. 4. (a) and (b). While $B_z(\uparrow)_{\text{eff}}$ is within a narrow resonant region, the balance between the clockwise θ_{K+} and anti-clockwise θ_{K-} Kerr-rotation components is broken, with the former dominating the process. It is notable that the energy difference between the spin-up and spin-down sub-bands is small as shown in Fig. 1(a)-SET, and is mostly induced by the loss of spatial inversion symmetry. Therefore, the resonance condition is limited to a narrow $B_z(\uparrow)_{\text{eff}}$ range (Fig. 4(b)). As a result, a steep Kerr-rotation appears. When $B_z(\uparrow)_{\text{eff}}$ is further increased beyond the resonant region, the efficiency of both θ_{K+} and θ_{K-} transitions decreases, resulting in disappearance of the signal (Fig. 4 (c)).

When the magnitude of the magnetic field is decreased, the system undergoes the reverse change. However, once the SET phase is magnetized by a combination of the external magnetic field, the return path (2→5) is different³⁰: the magnetic moment $M_z(\uparrow)$ due to the magnetization must be added to $B_z(\uparrow)_{\text{eff}}$. Therefore, when $B_z(\uparrow)_{\text{ex}}$ is decreased from “2” to “3”, the resonance condition is not attained at the same $B_z(\uparrow)_{\text{ex}}$ as for the outward path (position 1), resulting in hysteresis at position 3 (Fig. 4 (d)). From 3 to 5, the residual magnetization is gradually lost through scattering processes when $B_z(\uparrow)$ is decreased. Finally, the spin (up and down) density balance recovers alongside with time reversal symmetry at $B_z = 0$. As a result, along the return path the Kerr-rotation angle has a peak at lower applied

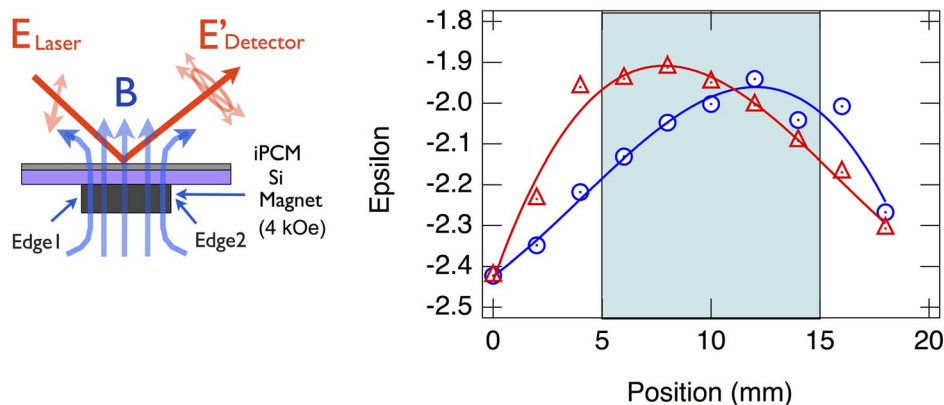


Figure 3 | Dielectric constant obtained from ellipsometric measurements using a wavelength of 633-nm. A $10 \times 10 \text{ mm}^2$ permanent magnet (4 kOe) was placed under the sample (left), and the dielectric constant at 633-nm was measured across the sample including areas above the magnet and on both sides (right). Blue and red curves represent the magnetic polarities N and S pointing up, respectively. The color section in light blue is the region, which the magnet was placed.

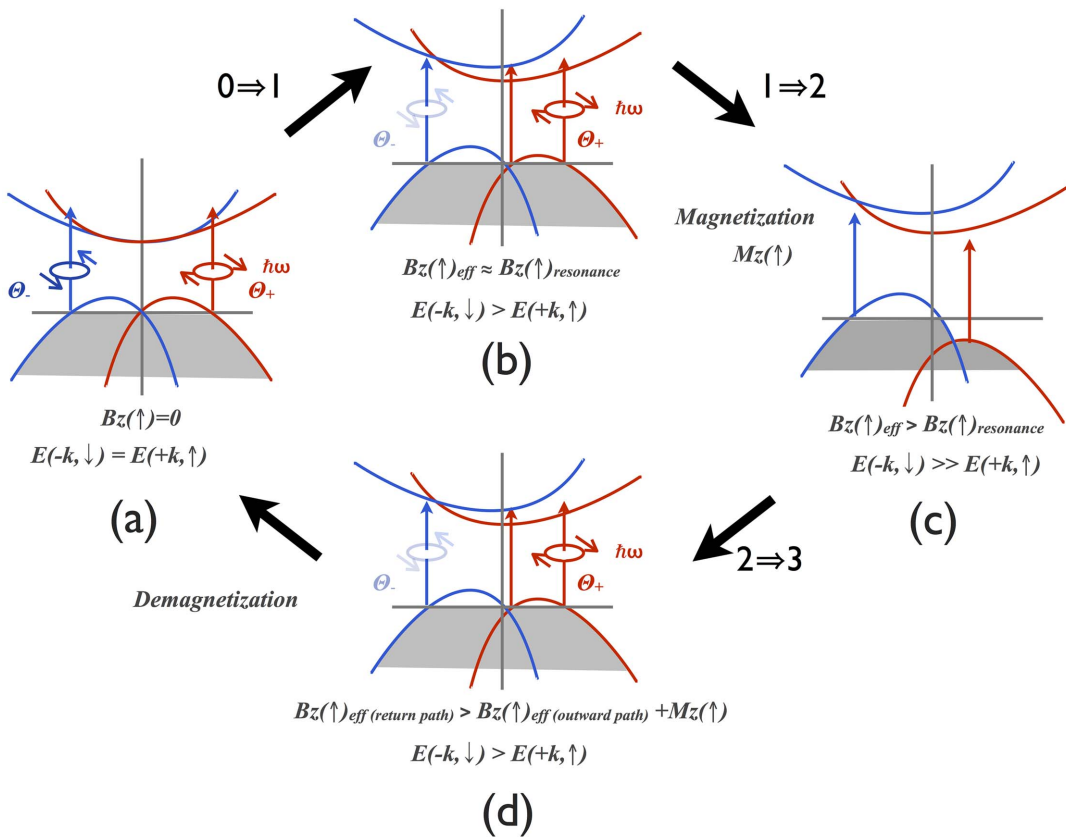


Figure 4 | The basic Kerr-loop mechanism of the SET phase. (a) Splitting into two spin-bands in the presence of time reversal symmetry in the SET phase at zero magnetic field $B_{zex} = 0$. The clockwise and anti-clockwise Kerr-rotation components cancel each other. (b) Resonance state due to $E(+k_x, \uparrow)$ at $B_z(\uparrow)_{resonance} = B_z(\uparrow)_{eff}$. (c) Non-resonance state when $B_z(\uparrow)_{eff} > B_z(\uparrow)_{resonance}$. (d) Resonance state on the return path. As the SET phase is once magnetized with $M_z(\uparrow)$ on the outward path, the return resonance state appears at a lower external magnetic field than $B_z(\uparrow)_{ex}$ on the outward path. The details depend on the band structure and the value of the magnetic field applied, as illustrated by the four panels. The notations 0, 1, 2, 3, and 4 correspond to the positions marked with the same indices in Fig 2(a).

magnetic field and decreases less abruptly compared with the onward path (Fig. 4 (a)).

We now turn to the important issue of the mirror symmetry of the Kerr-loop. The off-diagonal elements in the dielectric tensor ϵ_{ij} are proportional to the transition probabilities of the electrical dipole polarization operators P_+ or P_- between energy bands, and the Kerr- and Faraday-rotation can be calculated from the summation \mathcal{A} of individual oscillator strengths, $(f_{\pm})_{mn} = \alpha \cdot \omega_{mn} |P_{\pm}|^2$, i.e. $\mathcal{A} = \sum \{(f_+)_m n - (f_-)_m n\}$, where m, n, ω_{mn} and α are the band labels, the resonance frequency between m -th and n -th bands, and a constant, respectively³¹. Generally in magnetic materials, the sign of \mathcal{A} does not reverse with the polarity of the external magnetic field. As a result, a normal magnetic hysteresis loop is generated from the off-diagonal elements, $\epsilon_{yx} = -\epsilon_{xy}$ ¹⁶.

We note that if the Kerr rotation in the SET phase is driven by broken time-reversal symmetry due to the magnetic field, the Kerr rotation should change sense when the magnetic field is flipped. It suggests that the present Kerr signal is due to the presence of gyrotrropic order in the iPCM-SET phase, which has recently been discussed for cuprate superconductors^{32,33} and 1T-TiSe₂³⁴; in the latter it was associated with charge density waves. Gyrotrropic order breaks mirror symmetry, which causes optical activity. In the present case, mirror symmetries with respect to any plane perpendicular to the surface should be absent, because such symmetry makes the Kerr rotation signal for normal incidence to be an odd function of the magnetic field.

The next question is where the gyrotrropic order originates from. The facts that the sense of the Kerr rotation in the SET phase randomly varies among different nominally similar samples, while

for each sample the signal is perfectly reproduced when the sample is cooled down to the RESET phase and warmed up again to the SET phase suggests that the gyrotrropic order (handedness) is determined by the superlattice structure itself, rather than by spontaneous ordering of electronic states. We associate the presence of gyrotrropic order with the sequence of Ge and Te planes in the GeTe block of the SET phase. Indeed, while the rhombohedral structure of GeTe is often described as distorted cubic, it should be noted that there is a pronounced bond length (energy) hierarchy with the shorter Ge-Te bonds of 2.80 Å and longer Ge-Te bonds of 3.13 Å. Consequently, in a hexagonal representation the structure can be seen as layered with covalently bonded layers held together by weaker van-der-Waals interaction (Fig. 5(a)). The unit cell contains three covalently bonded layers with the Ge (marked using different colors for different layers) positions varying among the three layers. Shown in Fig. 5(b) is a GeTe unit cell with additional Ge atoms along the c axis. In the figure, the Ge atoms are connected by “bonds” that serve to guide the eye. One can clearly see that the Ge atoms form a helix oriented along the c-axis, i.e. along the propagation direction of the light. The Ge helix is further visualized in Fig. 5(c), where a view from a different angle is presented. Based on this model, the mirror symmetric Kerr rotation is expected in the SET phase.

Spatial inversion symmetry of the RESET phase (and of its GeTe block in particular) prevents the formation of helices in the latter. It should also be noted that while the existence of the mirror symmetric Kerr rotation per se arises from the presence of helical fragments, its resonant nature is a result of the Zeeman splitting by the magnetic field and the breaking of the spatial inversion symmetry; with both the helical fragments and the resonant band splitting being essential

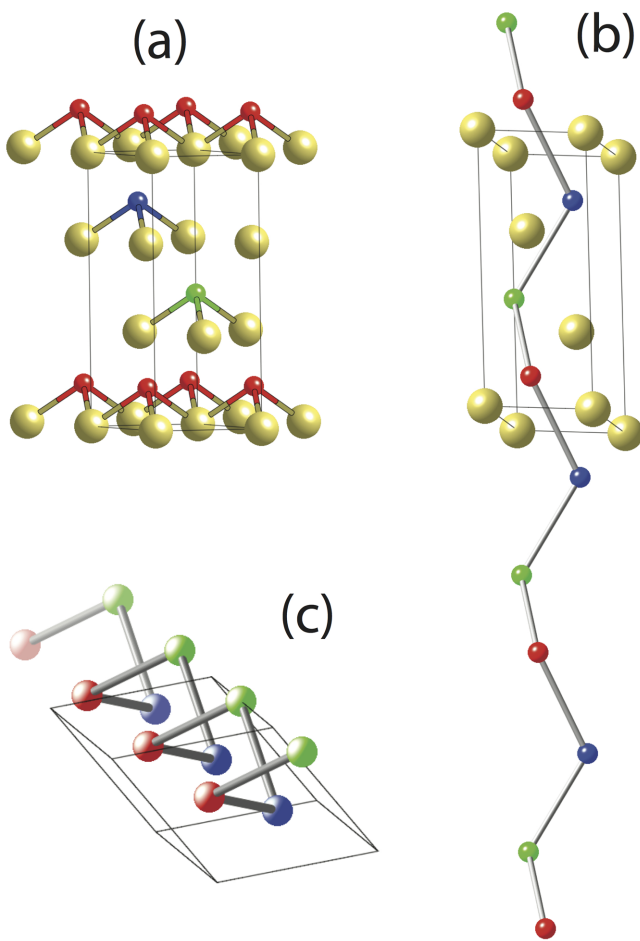


Figure 5 | (a) GeTe in a hexagonal representation. Te atoms are shown in tan and three inequivalent Ge atoms are shown in red, green, and blue. The shorter Ge-Te bonds within covalently bonded layers are shown as dual-band cylinders and the unit cell is shown as black lines. (b) The unit cell of GeTe with several additional Ge atoms along the c-axis. The Ge atoms are connected by gray lines to guide the eye. One can see that the Ge atoms form a helix. (c) A view on the Ge helix from a different angle. Only the Ge atoms and the unit cell are shown. Te atoms are invisible to make the helical structure unobscured.

attributes of the SET phase. Further work is underway to elucidate this issue in more details.

In conclusion, although iPCM superlattices were first designed for reduce the switching energy in memory devices, the present work demonstrates that they may become an interesting platform for experimental investigations of topological properties in engineered structures. The reversible band gap control by an external electric field in the RESET phase, and the spin-split band in the SET phase existing in iPCMs at different temperatures are highly attractive for applications beyond nonvolatile memory.

Methods

Fabrication of iPCM films. iPCM films were fabricated on Si wafers ($13 \sim 17 \Omega \cdot \text{cm}$) using a helicon-wave sputtering system that features a large (200 mm) target-substrate separation. The individual layers composing the $(\text{GeTe})_x/(\text{Sb}_2\text{Te}_3)_y$ structure were fabricated using GeTe and Sb_2Te_3 composite targets (2-inch) using an automated shutter control system with a substrate temperature of more than 500 K and pressures less than 0.5 Pa Ar. The unit thickness of the (GeTe) and (Sb_2Te_3) layers were 0.4 nm and 1.0 nm, respectively. To ensure strong crystalline orientation, a 5-nm thick Sb_2Te_3 layer was deposited prior to the fabrication of iPCM films. As a consequence, all the sub-layers were crystalline in the as-deposited state and exhibited a strong preferred crystallographic orientation towards the $\langle 111 \rangle$ direction. Finally, a 20-nm thick $\text{ZnS}-\text{SiO}_2$ layer was deposited as a cap layer to protect the films from oxidation.

Measurements. The film resistance was measured in plane using a two-probe system equipped with a small heater-stage. As electrodes, 50-nm thick W films were deposited at the sample edges. Most of the Kerr rotation measurements were performed using a linear polarized laser beam, with 690-nm wavelength & 500 μm spot size, incident at an angle of 4 degrees from the normal to the sample surface. The sample was set on a heater stage surrounded by a magnetic coil (maximum field: ± 13 kOe). The initial magnetic field was zero and the magnetic field change was in the following sequence: 0 kOe \rightarrow +13 kOe \rightarrow 0 kOe \rightarrow -13 kOe \rightarrow 0 kOe. Since this system did not allow us to change the wavelength, we used a different system for measurements using 650-nm and 400-nm light. In the latter the magnetic field was swept not from zero but from the maximum positive to maximum negative values and back, namely, +10 kOe \rightarrow 0 kOe \rightarrow -10 kOe \rightarrow 0 kOe \rightarrow +10 kOe. The optical dielectric constant was measured by an ellipsometer equipped with a He-Ne laser (633-nm wavelength). The magnetic field was applied to the sample using a 1 mm thick flat square permanent magnet (10 mm \times 10 mm area) with a 4 kOe field. The laser beam was scanned every 2 mm to measure the optical parameters in between the sample edges.

Simulation of the SET&RESET models and the corresponding band structures. The electronic band structures of the iPCM films were simulated using two *ab-initio* simulation codes: CASTEP and WIEN2K. iPCM models were first relaxed using the plane wave code CASTEP with a GGA exchange correlation term as constructed by Perdew-Burke-Ernzerhof (PBE). A $4 \times 4 \times 1$ Monkhorst-Pack grid was used for integration and ultrasoft pseudopotentials were used with a cutoff energy of 230 eV^{35,36}. After 0 K Broyden geometrical optimization, the models were transferred to WIEN2K³⁷ to include spin-orbit coupling effects. Wien2K is an all electron code that uses a linearized augmented plane wave + local orbital (LAPW + lo) basis within density-functional theory. The PBE exchange-correlation was used. A Monkhorst-Pack grid of $4 \times 4 \times 1$ was used for integrations in the Brillouin zone and a $R_{\text{K}_{\text{max}}} = 7.0$ value was used for the plane wave component of the plane-wave basis used between augmentation spheres.

1. Moore, J. E. The birth of topological insulator. *Nature* **464**, 194–198 (2010).
2. Bernevig, B. A., Hughes, T. L. & Zhang, S.-C. Topological Phase Transition in HgTe Quantum Wells. *Science* **314**, 1757–1761 (2006).
3. Hsieh, D. *et al.* A topological Dirac insulator in a quantum spin Hall phase. *Nature* **452**, 970–975 (2008).
4. Xia, Y. *et al.* Observation of a large-gap topological-insulator class with a single Dirac cone on the surface. *Nat. Phys.* **5**, 398–402 (2009).
5. Hsieh, D. *et al.* A tunable topological insulator in the spin helical Dirac transport regime. *Nature* **460**, 1101–1106 (2009).
6. Hsieh, D. *et al.* Observation of time-reversal-projected single-Dirac-cone topological-insulator states in Bi_2Te_3 and Sb_2Te_3 . *Phys. Rev. Lett.* **103**, 146401 (2009).
7. Zhang, H. *et al.* Topological insulators in Bi_2Se_3 , Bi_2Te_3 and Sb_2Te_3 with a single Dirac cone in the surface. *Nat. Phys.* **5**, 438–442 (2009).
8. Kim, M., Kim, C.-H., Kim, H.-S. & Ihm, J. Topological quantum phase transitions driven by external electric fields Sb_2Te_3 in thin films. *PNAS* **109**, 671–674 (2011).
9. Simpson, R. *et al.* Interfacial phase-change memory. *Nat. Nano.* **6**, 501–505 (2011).
10. Tominaga, J., Kolobov, A. V., Simpson, R. & Fons, P. Theoretical and experimental studies on superlattice $\text{Ge}_3\text{Sb}_2\text{Te}_5$. In *Proceedings of the European Symposium on Phase Change and Ovonic Science* (EPCOS, Aachen, Germany), pp. 148–150 (2009).
11. Sa, B., Zhou, J., Sun, Z., Tominaga, J. & Ahuja, R. Topological Insulating in $\text{GeTe}/\text{Sb}_2\text{Te}_3$ Phase-Change Superlattice. *Phys. Rev. Lett.* **109**, 096802 (2012).
12. Tominaga, J. *et al.* Ferroelectric Order Control of the Dirac-Semimetal Phase in $\text{GeTe}-\text{Sb}_2\text{Te}_3$ Superlattices. *Adv. Mater. Interfaces* **1**, 1300027 (2014).
13. Tominaga, J., Simpson, R., Fons, P. & Kolobov, A. V. Electrical-field induced giant magnetoresistivity in (non-magnetic) phase change films. *Appl. Phys. Lett.* **99**, 152105 (2011).
14. Qi, X.-L. & Zhang, S.-C. Topological insulators and superconductors. *Rev. Modern Phys.* **83**, 1057–1110 (2011).
15. Shi, V. *et al.* Spatial imaging of the spin Hall effect and current-induced polarization in two-dimensional electron gases. *Nat. Phys.* **1**, 31–35 (2005).
16. Mansuripur, M. *The physical principles of magneto-optical recording* (Cambridge Univ. Press, Cambridge, 1998).
17. Tse, W.-K. & MacDonald, A. H. Magneto-optical Faraday and Kerr effects in topological insulator films and in other layered quantized Hall systems. *Phys. Rev. B* **84**, 205327 (2011).
18. Tse, W.-K. & MacDonald, A. H. Giant magneto-optical Kerr effect and universal Faraday effect in thin film topological insulators. *Phys. Rev. Lett.* **105**, 057401 (2010).
19. Siegrist, T. *et al.* Disorder-induced localization in crystalline phase-change materials. *Nat. Mater.* **10**, 202–208 (2011).
20. Wel, P. *et al.* Exchange-Coupling-Induced Symmetry Breaking in Topological Insulators. *Phys. Rev. Lett.* **110**, 186807 (2013).
21. Yokoyama, T. & Tserkovnyak, Y. Spin diffusion and magnetoresistance in ferromagnet/topological-insulator junctions. *arXiv:1310.3354v1* (2013).
22. Nan, C.-W. *et al.* Multiferroic magnetoelectric composite: historical perspective, status, and future directions. *J. Appl. Phys.* **103**, 031101 (2008).



23. Cherifi, R. O. *et al.* Electric-field control of magnetic order above room temperature. *Nat. Mater.* **13**, 345–351 (2014).
24. Sanchez, J. C. R. *et al.* Spin-to-charge conversion using Rashba coupling at the interface between non-magnetic materials. *Nature Commun.* **4**, 2944; DOI: 10.1038/ncomms3944 (2014).
25. Zyuzin, A. A. & Burkov, A. A. Thin topological insulator film in a perpendicular magnetic field. *Phys. Rev. B* **83**, 195413 (2011).
26. Tahir, M., Sabeeh, K. & Schwingenschlögl, U. Quantum capacitance of an ultrathin topological insulator film in a magnetic field. *Nat. Sci. Rep.* **3**, 126; DOI: 10.1038/srep01261 (2013).
27. Analytis, J. G. *et al.* Two-dimensional surface state in the quantum limit of a topological insulator. *Nat. Phys.* **6**, 960–964 (2010).
28. Chen, Y. L. *et al.* Massive Dirac Fermion on the Surface of a Magnetically Doped Topological Insulator. *Science* **329**, 659–662 (2010).
29. Zhou, J. J. *et al.* Engineering Topological Surface States and Giant Rashba Spin Splitting in BiTeI/Bi₂Te₃ Heterostructures. *Nat. Sci. Rep.* **4**, 3841; DOI: 10.1038/srep03841 (2014).
30. Tominaga, J. *et al.* Spin-storage mechanism in interfacial phase-change memory (PCM). In *Proceedings of the European Symposium on Phase Change and Ovonic Science* (EPCOS, Berlin, Germany), pp. 5–7 (2013).
31. Davydov, A. S. *Quantum Mechanics* (Pergamon, Oxford, 1965).
32. Orenstein, J. & Moore, J. E. Berry phase mechanism for optical gyrotropy in stripe-ordered cuprates. *Phys. Rev. B* **87**, 165110 (2013).
33. Hosur, P., Kapitulnik, A., Kivelson, S. A., Orenstein, J. & Raghu, S. Kerr effect as evidence of gyrotropic order in the cuprates. *Phys. Rev. B* **87**, 115116 (2013).
34. Ishioka, J. *et al.* Chiral Charge Density-Waves. *Phys. Rev. Lett.* **105**, 176401 (2010).
35. Martin, R. M. *Electronic Structure-Basic theory and practical methods* (Cambridge Univ. Press, Cambridge, 2004).
36. Vanderbilt, D. Soft self-consistent pseudopotentials in a generalized eigenvalue formalism. *Phys. Rev. B* **41**, 7892–7895 (1990).
37. Schwarz, K. & Blaha, P. Solid state calculations using WIEN2K. *Comp. Mater. Sci.* **28**, 259–273 (2003).

Acknowledgments

A part of the work was supported by FIRST program initiated by the Council for Science and Technology Policy (CSTP) and by TIES, MEXT Elements Strategy Initiative to Form Core Research Center (S.M.). We wish to thank Ms. Reiko Kondou for her assistance in the fabrication of iPCMs.

Author contributions

J.T. designed the experiments. J.T. and Y.S. fabricated the iPCM superlattice films. A.G. and R.C. fabricated the epi-GeTe film. D.B., H.A., Y.S., K.M., T.N. and J.T. performed the magneto-optical & resistance experiments. M.H., Y.T., A.K., P.F., J.T. and S.M. contributed the theoretical discussions. K.M. and T.N. assisted the analysis. Finally, J.T. and A.K. wrote the paper.

Additional information

Supplementary information accompanies this paper at <http://www.nature.com/scientificreports/>

Competing financial interests: The authors declare no competing financial interests.

How to cite this article: Bang, D. *et al.* Mirror-symmetric Magneto-optical Kerr Rotation using Visible Light in [(GeTe)₂(Sb₂Te₃)₁]_n Topological Superlattices. *Sci. Rep.* **4**, 5727; DOI:10.1038/srep05727 (2014).

 This work is licensed under a Creative Commons Attribution-NonCommercial-NoDerivs 4.0 International License. The images or other third party material in this article are included in the article's Creative Commons license, unless indicated otherwise in the credit line; if the material is not included under the Creative Commons license, users will need to obtain permission from the license holder in order to reproduce the material. To view a copy of this license, visit <http://creativecommons.org/licenses/by-nc-nd/4.0/>